HINDER
Holistic Integration of Navigational Dynamics for Erosion Reduction

NASA Human Lander Challenge (HuLC) 2024
Mitigation of Plume-Surface Interactions

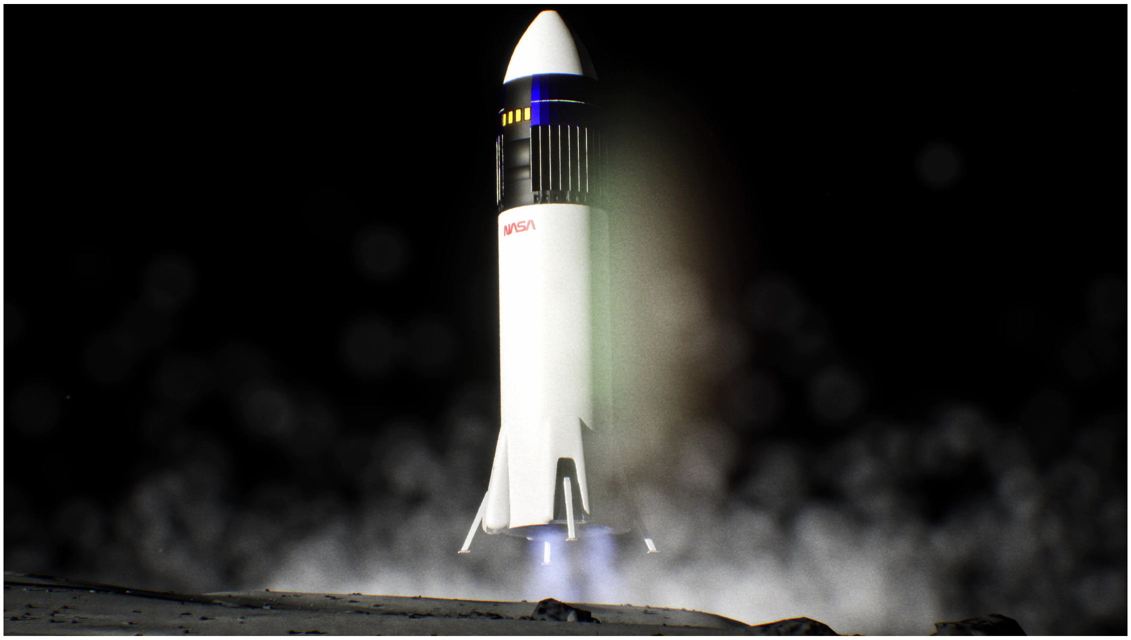

Department of Aerospace Engineering
Grainger College of Engineering
University of Illinois Urbana-Champaign

Project Mananger: Shikhar Kesarwani, Junior, Aerospace Engineering
Faculty Advisors: Laura Villafañe Roca, Ph.D
Graduate Student Advisor: Nicolas Rasmont, Ph.D candidate

Team Members

Ishaan Bansal*
Junior
Aerospace Engineering

Aparna Kamath
Sophomore
Physics

Ethan Kooper
Freshman
Physics

Brody Lauer
Senior
Aerospace Engineering

Chen Li
Senior
Aerospace Engineering

Krisha Mahajan
Junior
Mechanical Engineering

Benjamin Ochs
Sophomore
Aerospace Engineering

Adam Pawlik**
Sophomore
Mechanical Engineering

Galen Sieck
Junior
Aerospace Engineering

Cliff Sun
Freshman
Physics & Math

Sahilkrishna Vazhatodhyil
Sophomore
Aerospace Engineering

*Landing Optimization Team Lead
**Instrumentation Team Lead

HINDER: Holistic Integration of Navigational Dynamics for Erosion Reduction

The University of Illinois Urbana-Champaign

HUMAN LANDER CHALLENGE

Major Objectives & Technical Approach

- Mitigate surface erosion and ejecta during landing
- Implement a low cost and high TRL system, which can be developed and implemented within 3-5 years
    - Integrate into existing interfaces where possible
- Target unprepared and undeveloped landing sites, with a focus on developing lander agnostic solutions
    - Limit designs to allow for testing and implementation on CLPS landers in addition to HLS
- No additional risks posed to crew or surface infrastructure
    - Retire as much risk as possible prior to launch

Concept of Operations:

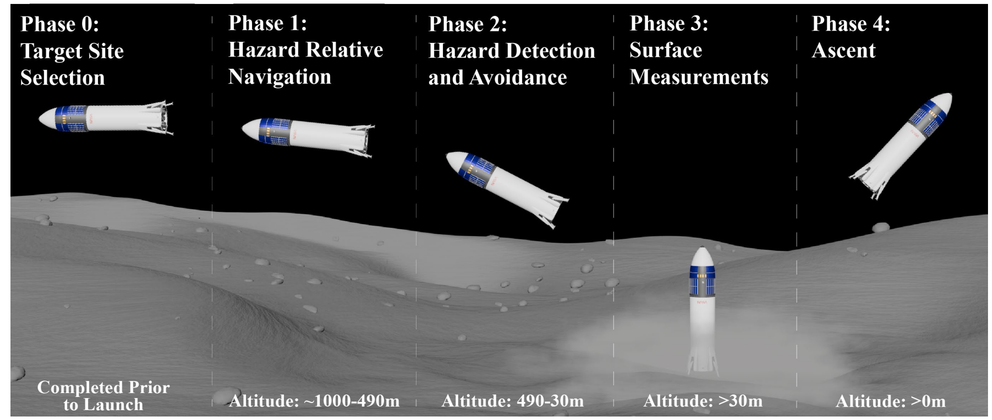

Key Design Details

HINDER uses a 3 phase approach to select landing sites which reduced PSI effects in the absence of dedicated infrastructure:

- Use existing radar data to map bulk density before launch
- Use state of the art radar to measure soil characteristics during landing to avoid unfavorable landing sites
- Reference simulations to quantify PSI effects of hazard avoidance

After landing, measure regolith characteristics to inform soil and erosion models

Concept Innovations

- Applying radar estimates of soil models to landing site selection
- Adaptation of existing radar systems for real time surface characteristic measurements during final descent

Schedule:

- Design and development begins in FY 2024
- Fabrication, integration and testing begins in FY 2025
- Pre-cursor launch in FY 2026 with Artemis III
- Final assembly and launch in FY 2028 with Artemis IV

Cost:

- Lower Estimate:
    - $1.36 million
- Upper Estimate:
    - $14.8 million

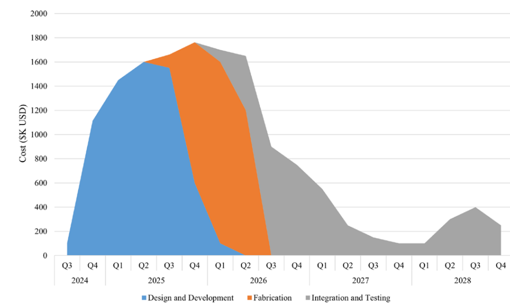

Contents

I. Introduction

The University of Illinois Urbana-Champaign proposes the Holistic Integration of Navigational Dynamics for Erosion Reduction (HINDER), a systems-level concept aimed at mitigating the risks of plume surface interactions (PSI) during final descent and landing. From mission planning through terminal descent to the lunar surface, HINDER supports landing site selection within regions of interest to reduce the risks associated with surface erosion and ejecta due to the thruster plume(s) impingement on the surface. To accomplish this, candidate landing sites with high bulk soil density are first identified through remote sensing using pre-existing orbital assets, and high bulk density is correlated with lesser surface erosion. During landing, a radar instrument onboard HLS is used during refine local bulk density estimates with higher resolution and identify a more precise landing site. By integrating this approach into the existing Precision Landing and Hazard Avoidance (PL&HA) system with consideration of the impact of a divert on PSI erosion and cratering, an optimal descent trajectory can be implemented to reduce risks to the Artemis missions. With this approach, HINDER is both lander agnostic and has small size, weight, and power (SWaP), providing the flexibility to mitigate the effects of PSI for a wide range of locations and landers.

II. System Overview

A. Requirements

The 2024 Human Lander Challenge (HuLC) requirements are adapted into high level mission requirements as listed in Table 1 and are all met by our proposed solution. Based on stakeholder interest in implementing a solution in a short time frame regardless of the presence or absence of surface assets, HINDER focuses on mitigating the effects of PSI at unprepared landing sites for HLS. Additionally, while not a strict requirement, HINDER is designed to not interfere with other PSI instrumentation systems, such as the PSI Lunar Measurement System (PLUMES) [1].

Table 1 HINDER System Requirements

Identifier	Requirement
MR-01	HINDER shall mitigate the effects of Plume Surface Interaction.
MR-02	HINDER shall be capable of implementation in ≤ 5 years.
MR-03	HINDER shall function in a cislunar environment.
MR-04	HINDER shall function with no assumption of pre-existing surface assets.
MR-05	HINDER shall be able to be integrated on any HLS lander.

B. Concept of Operations

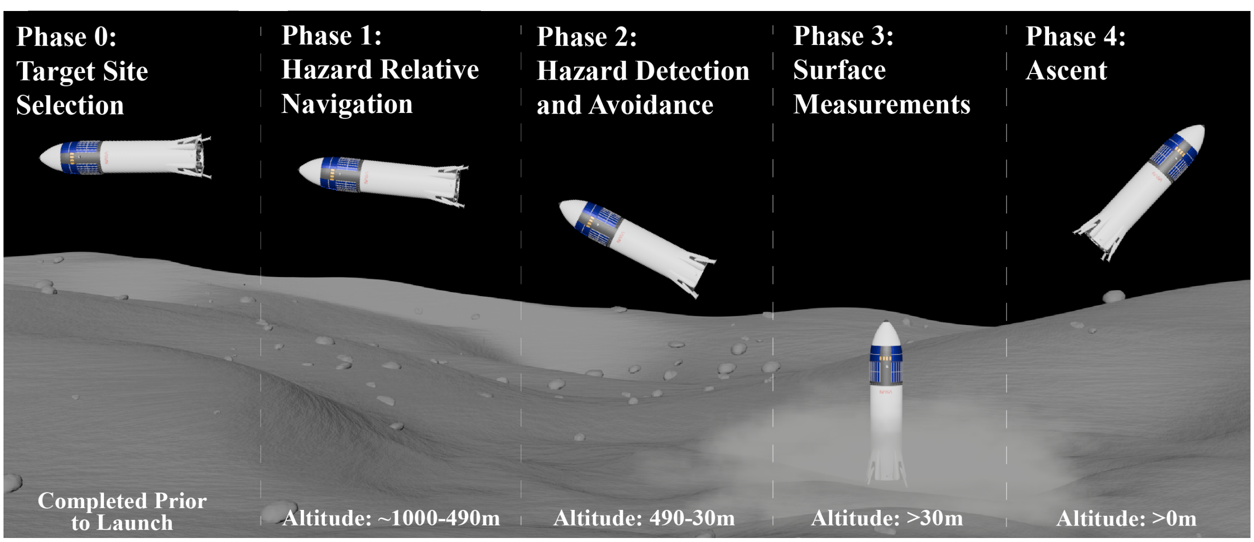

Fig. 1 HINDER Concept of Operations

HINDER commences with Phase 0 taking place on Earth, prior to the launch of any elements of the HLS mission. Using maps of soil parameters derived from sensor data taken by the Lunar Reconnaissance Orbiter and Chandryaan-2, areas with high risk for increased surface erosion can be identified and avoided during site selection. To further refine the results of Phase 0 which is completed on Earth, Phase 1 is completed during flight above the Moon an uses a radar instrumentation system to image the surface underneath the lander within the pre-selected landing zone. Radar data transmitted and received in real-time during descent is compared against existing maps to ensure nominal radar performance and positioning. This data is stored locally to then used to measure the change in radar response of the landing spot before and after PSI. This operation is done to add to NASA's current terrain relative navigational capabilities, filling an existing gap within its precision landing and hazard avoidance (PL&HA) suite. Phase 2 is Hazard Detection and Avoidance (HDA). In Phase 2, the instrumentation system identifies PSI hazards in real-time by measuring soil parameters correlated with adverse PSI effects to the lander or nearby surface assets. Particularly, it measures soil dielectric constant with radar and uses this to estimate surface soil bulk density. As the lander's altitude decreases and instrument surface resolution increases, the instrumentation system down-selects to landing sites with higher surface soil density and creates a high-resolution soil density map. To choose a final landing site, the onboard avionics combines data from the integrated Precision Landing & Hazard Avoidance (PL&HA) system and the resultant density map. After a final landing site has been selected, the system diverts to it and progresses to Phase 3: Surface Measurements. The instrumentation system remains active during terminal descent, measuring changes in dielectric constant during active erosion to collect data and inform soil models. After surface operations are complete, Phase 4 begins and the instrumentation system measures changes in landing site soil parameters during the lander's ascent to study the effects of PSI during takeoff.

It is important to note that the current concept of operations differs slightly from the initial HINDER proposal. Phase 1 and Phase 2 are altered to introduce a new terrain-relative navigation capability —referred to as hazard relative navigation within the context of highly PSI-susceptible landing sites —to this system. This new capability enables the system to match the hazard map generated in flight to the hazard map generated before flight, reducing risk and allowing the flight radar to skip imaging areas which are known to be hazardous. Altitude changes for each phase are due to operational and hardware limitations, including a new instrumentation system design which constrains Phase 2 to be performed below the threshold of 490 m.

C. Developmental Timeline

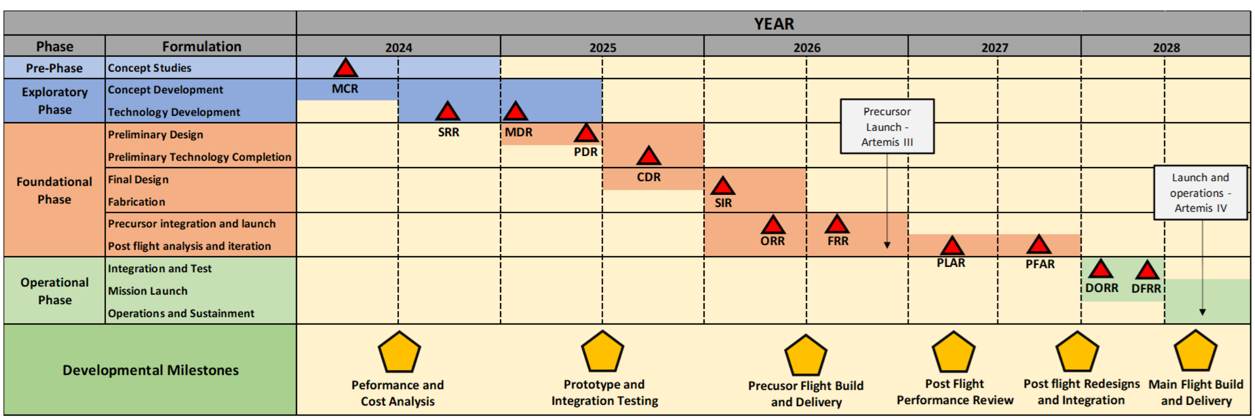

Fig. 2 HINDER Review Timeline

The developmental timeline of HINDER is split into three phases: Exploratory, Foundational, and Operational. The Exploratory phase begins in Fiscal Year (FY) 2024, focusing on concept and technology development. During this phase, Mission Concept and System Requirements Reviews are conducted to outline the mission architecture and evaluate the proposed objectives and strategies for achieving them. The Foundational phase starts in FY 2025 and lasts until the end of FY 2027. Preliminary and Critical Design Reviews prior to fabrication are conducted in FY 2025. Integration and testing are planned for FY 2026 with the aim of developing a pathfinder to fly on a precursor mission. The pathfinder will operate in data collection mode during Artemis III in Q4 FY 2026. The Operational phase begins in FY 2028 and concludes with the launch of Artemis IV. After the precursor mission, each aspect of HINDERs performance is evaluated in post-launch assessment and flight assessment review. Necessary changes are made to the final iteration of the system, which is then integrated into Artemis IV with full operational capability. The implementation of HINDER in further missions is anticipated to follow the outlined timeline from the Operations phase onwards. This timeline is based on NASA's PLUMES technology development plan, reflecting the similarity in scope and purpose between the two projects [1]. To address challenges faced by similar instruments, special emphasis is placed on experimental milestones, mainly testing and integration. The HINDER review timeline and technology readiness level (TRL) development schedule are shown in Fig. 2 and Fig. 3, respectively. The schedule is slightly delayed from the preliminary timeline in the earlier HINDER proposal, with the Artemis III mission being switched from the first full operation of HINDER to a data collection flight. The additional time between Artemis III and Artemis IV allows for any issues identified with integration and opertion on Artemis III to be resolved.

YEAR	2024	2025	2026	2027	2028
Phase	Exploratory Phase	Foundational Phase			Operational Phase
HINDER Mission Planning	Concept and Technology Development	Pathfinder Minimum Viable Experiment and Product			Mission Deliverable
	Focus is on further plume surface interaction model research, trade studies into component selection, and initial prototyping of hardware and software. Collaborations with Universities, research institutions, and private corporations are seeked out.	A pathfinder is developed to be extensively tested on point-to-point terrestrial lander testbeds and high-velocity aircraft. Success found in preliminary tests will result in a more robust pathfinder to be integrated on and demonstrated with a precursor mission to verify all associated technologies and models. The pathfinder is augmented with additional assets for successful integration onto HLS and be capable of running on a data-collection mode during Artemis III			HINDER's performance from Artemis III is evaluated and any necessary design changes to subsystems are performed. A final iteration is created to be integrated into Artemis IV will full operational capability.
TRL	1 - 3	4 - 5	6 - 7	8	9

Fig. 3 HINDER Developmental and Operations Timeline

D. Modeling and Validation

The primary effects of PSI impacting mission safety are ejecta dynamics, crater erosion, and the aerodynamics of plume impingement. However, these effects are coupled. Because of this, only crater erosion is quantified in this analysis with the assumption that mitigating this factor also results in mitigated ejecta impacts and aerodynamic effects. To model crater erosion due to PSI, the analytical model developed by Leonard Roberts relating erosion rate to excess shear stress (Roberts' model) is used. This model is given in Eq. 1, and assumes that the erosion rate is determined by the excess shear stress available to accelerate soil particles to a proportion of the gas velocity [2, 3]. This equation is expanded on in Appendix XI.A.

$$\frac{\partial y}{\partial t} = \frac{2(\tau - \tau^*)}{au \cdot \sigma c \cdot \cos(\beta)} \tag{1}$$

In this model, τ is the shear stress, τ^* is the restraining shear stress, β is the local slope angle, σc is the surface bulk density, u is the gas radial velocity, and a is the fraction of the gas velocity that the particle achieves such that the final particle velocity is au [2, 4]. Roberts' model assumes a single vertically oriented jet where the primary mode of erosion is due to the viscous flow on the surface exerting a shear force on the top layer of the soil. Other diffusion driven flow erosion models were also considered. In these models, the primary mode of erosion is caused by the diffusion of the jet exhuast flow into the surface acting a lift force on the granular material [5, 6]. In Roberts' model, this diffusion driven erosion is not considered, as the assumption is made that the shear forces outweigh the gas diffusion. While Roberts' model is not as accurate as modern predictive models or CFD simulations, it is sufficient for a preliminary demonstration of methods that can be applied with other models [7, 8]. It can also be used to identify driving variables for PSI which can later be confirmed by the more complex models and simulations.

III. Target Site Selection

A. PSI Impact Mitigation Strategy

In the interest of predicting PSI-related hazards to landing and avoiding sites vulnerable to these hazards in mission planning prior to flight, surface characteristics impacting erosion rate are identified through Roberts' model to be bulk density (σc), particle size (D), and soil shear strength (τ^*). Based on this model, increasing the soil bulk density, particle size, and shear strength decreases the rate of erosion under PSI. Experimental results such as the Mauna Kea lunar test and in-situ observations on the Apollo missions further support these conclusions [9, 10]. Newer models of erosion such as the ones derived by Metzger also feature an inverse relationship between erosion rate and bulk density [5, 6]. In order to remotely estimate these parameters from a long range prior to landing in order to characterize the most hazardous sites, HINDER focuses on estimating regolith bulk density. This is because through the strong correlation between soil bulk density and soil bulk density, the bulk density can be estimated for large parts of the lunar surface using existing data without the need to launch additional instrumentation. While particle size and soil shear strength are useful in identifying sites hazardous to landing, they are less easily derived from existing data sets and so they are beyond the scope of this analysis. As a preliminary bound on the expected range of bulk density, the density values measured by Apollo 17 core samples range from 1.57 g/cm^3 to 2.29 g/cm^3, which is a variation of over 30% in local bulk density values [9]. Across all Apollo missions, the samples collected ranged from densities of 0.75 g/cm^3 to a maximum of 2.29 g/cm^3 [9].

The key benefit of using remote sensing to identify and avoid hazardous terrain during mission planning is that it is preventive: providing significant improvements to safety while remaining minimally invasive to the overall system. HINDER does not require the pre-positioning of any assets on or around the Moon, which both enables a more rapid path to implementation and enables its use for rarely-visited sites where permanent infrastructure, such as landing pads, is not justifiable. It also does not interfere with any other PSI instrumentation on the lander or directly impact the surface in any way that could compromise scientific research after landing. Instead, the identification of PSI hazards prior to launch allows some level of PSI risk to be mitigated without any modification to flight systems.

B. Bulk Density Estimation Method

In order to remotely estimate bulk soil density from existing data, HINDER uses the strong correlation between bulk density and the dielectric constant of the surface regolith [12]. For lunar regolith, the dielectric constant ε' is approximately related to the soil bulk density ρ (in g/cm^3) by the relation $\varepsilon' = (1.92)^\rho$ [11–14]. By measuring the dielectric constant of the lunar surface using current and past orbiters, regolith bulk density is estimated to a sufficient precision such that areas with less favorable surface properties with higher erosion susceptibility can be identified. These areas can then be classified as PSI hazards and factored into the landing site selection prior to launch from Earth. This relationship between dielectric constant and bulk density is independent of composition, which enables site assessments to be made with a single measurement even in the absence of information about the composition of the regolith. The correlation is close enough to reasonably identify hazards within the landing area but lacks the precision needed to optimize site selection between similar candidate sites.

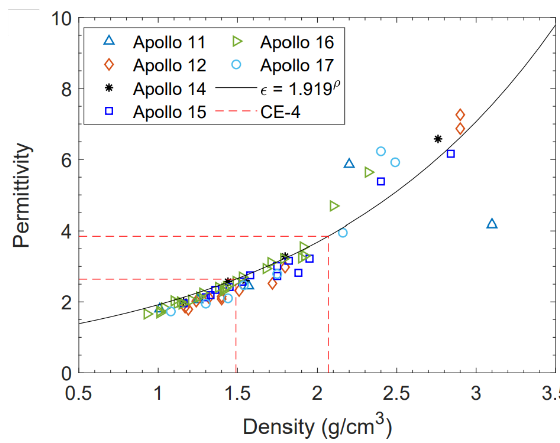

Fig. 4 Correlation Used for Lunar Regolith Bulk Density Estimation [11]

While dielectric constant cannot be directly measured using remote sensing, multiple methods have been demonstrated to accurately estimate it using Synthetic Aperture Radar (SAR) data when compared against in-situ measurements such as those taken on Apollo 17. These methods include, but are not limited to, the Fresnel reflection coefficient model [14], a modified Campbell inversion model [15], a co-polarization ratio model [16], a hybrid polarimetric scattering similarity model [17], and a symmetric coherency and anisotropy model [18]. Due to the limits of this analysis only the symmetric coherency and anisotropy model described by Bhattacharya et al [18] and the modified Campbell inversion model described by Calla et. al [15] were replicated in Section III.D to demonstrate the potential of this concept.

C. Target Site Selection Using Existing Data (Phase 0)

Within the past year, the use of Mini-RF radar on the Lunar Reconnaissance Orbiter (LRO) to characterize bulk density with dielectric constant, specifically in the context of the Artemis III landing sites, has been suggested by Patterson et al. along with the Mini-RF team and Rivera-Valentín et al. [19, 20]. Given the experience of Patterson and the Mini-RF team and their prior work with NASA, it is likely that the models planned for this analysis would be well suited for implementation in HINDER. Additionally, Patterson et al. have identified that 10 of the 13 candidate Artemis landing zones have high-resolution (30 m per pixel) S-band data that can be used for this purpose, while the remaining sites are covered by lower resolution (100 m per pixel) data sets [20]. The novel proposal of HINDER is to apply this data to identify target landing sites which are less susceptible to PSI due to a higher local bulk density, allowing PSI to be mitigated without modification to any flight systems and completing before the lander itself even leaves Earth. The resolutions of current Mini-RF data sets are acceptable for identifying and comparing candidate landing targets within the broader landing zones since the HLS lander is intended to land within 100 m of a target [21]. When verifying the models applied in Section III.D, ground based Apollo measurements of dielectric constant above 4 were not included in the verification data set. This is because dielectric constant measurements of $\varepsilon' > 4$ are typically associated with individual rocks rather than bulk soils [9, 12].

D. Methods and Verification for Concept Demonstration

The first model replicated as a HINDER concept demonstration is the symmetric coherency and anisotropy model, developed by Bhattacharya et al. [18]. This model works by using the opposite sense radar backscatter coefficient from Synthetic Aperture Radar (SAR) measurements to estimate an anisotropy parameter for the regolith, which can then be used to bound the local dielectric constant [18]. This backscatter coefficient can be derived from the co-polarized scattered power, which is a function of the Stokes vector as described by Fa et al. [22]. The Stokes vector is a set of values that characterizes the radar polarization, and Stokes vector datasets are available as derived datasets of Mini-RF radar measurements. Additionally because radar returns can be significantly influenced by surface slope, the results are considered unreliable for slopes >10° (which are also beyond the landing constraints for HLS) [18]. Applying this process, the results from Bhattacharya et al. for the Apollo 17 site were replicated without masking slopes, as shown in Fig. 5b. This method was verified by the original authors by comparing the average dielectric constant calculated to the average value in the region [18]. However, the verification work performed for HINDER shows that the the relative trends of high and low dielectric constant produced by the model contradict the measurements taken during Apollo 17, as shown in in Fig. 5c. For this reason, the symmetric coherency and anisotropy model is not used for further analysis, but demonstrates the methods used to confirm the accuracy of a data processing method.

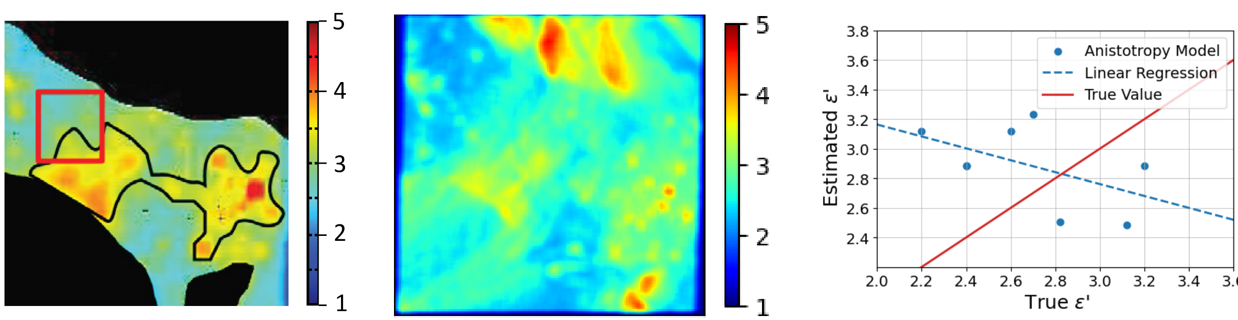

(a) Original Map from [18] **(b) Map from HINDER Code** **(c) Anisotropy Model Verification**

Fig. 5 Dielectric Constant from the Anisotropy Model for the Apollo 17 Site

The second model replicated as a HINDER concept demonstration is a modification of the Campbell inversion model. The Campbell inversion model given in Eq. 2 where ϕ is the look angle and σ^0_{HH} and σ^0_{VV} are the horizontal and vertical backscatter coefficients, respectively [12]. However, this model requires the use of polarized backscatter coefficients, which cannot be obtained from a hybrid polarized radar like Mini-RF. Instead, this analysis uses a modified version of the model which replaces the horizontal and vertical backscatter coefficients σ^0_{HH} and σ^0_{VV} with the circularly polarized equivalents, σ^0_{LH} and σ^0_{LV}, which is given in Eq. 3 [15]. This change significantly reduces the accuracy of the model but preserves many of the local trends and allows the data to be easily processed. For full implementation of HINDER by NASA, a different model is recommended.

$$\varepsilon' = \left(\sin(\phi)/\sin\left[\arccos\left(\frac{\sigma^0_{HH}}{\sigma^0_{VV}}\right)^{0.25} - \phi\right]\right)^2 \tag{2}$$

$$\varepsilon' = \left(\sin(\phi)/\sin\left[\arccos\left(\frac{\sigma^0_{LH}}{\sigma^0_{LV}}\right)^{0.25} - \phi\right]\right)^2 \tag{3}$$

For this analysis, we replicated the approach described by Callo et. al [15] of using hybrid polarimetric data from Mini-RF in a modified version of Campbell's inversion model given in Eq. 3. Our maps resulting from applying this approach to data from the Apollo 17 site are shown in Fig. 6. The trends in dielectric constant over the terrain largely matched the trends in Apollo 17 sample measurements [15, 17]. While there are still some significant errors in the dielectric constant estimation across these samples, these errors and imprecision are expected for a simplified model like this, while more advanced models such as the Fresnel coefficient model used by Kumar et. al [14] have demonstrated dielectric constant estimation errors of <5% for Apollo 17 sample sites. For the purposes of a HINDER concept demonstration, the modified Campbell inversion model is considered sufficient, though additional analysis with more accurate models as recommended by the Mini-RF team is required for effective landing site selection [19, 20].

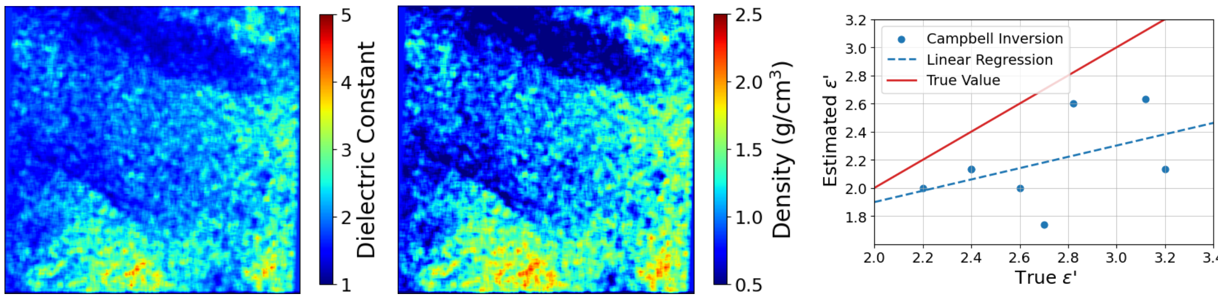

(a) Dielectric Constant **(b) Bulk Density (g/cm^3)** **(c) Campbell Model Verification**

Fig. 6 Campbell Inversion Model Results for the Apollo 17 Site

E. Concept Demonstration of Radar for Target Site Selection

Based on the relative success of the Campbell inversion model at identifying approximate trends and bounds in the local dielectric constant in Section III.D, the method is applied to candidate Artemis landing regions to estimate the local variation in regolith bulk density around these areas. The primary landing region analyzed is in the Haworth region, particularly in a flat area with slopes <10° due to HLS constraints [21]. This area is approximately 3 km by 3 km and is centered at 87.255°S and 338.8°E. This region is used as example of how this method can be generally applied to candidate landing regions to identify and avoid potentially hazardous sites in the mission planning process. Within this area, the regolith bulk density is estimated to vary significantly from about 0.8 g/cm^3 to 2.0 g/cm^3. As an example of the potential impact of this landing site selection method, there are two landing circles placed on Fig. 7, each about 200 m diameter based on HLS landing precision [21]. These landing sites are only about 300 m apart from center to center, but the average estimated bulk density within them varies from about 1.25 g/cm^3 to about 1.71 g/cm^3, a difference of 27%. By taking these differences into account during mission planning under the principle that higher local soil density leads to lower surface erosion under PSI, the impacts of PSI from HLS can be significantly mitigated without any modification to the lander.

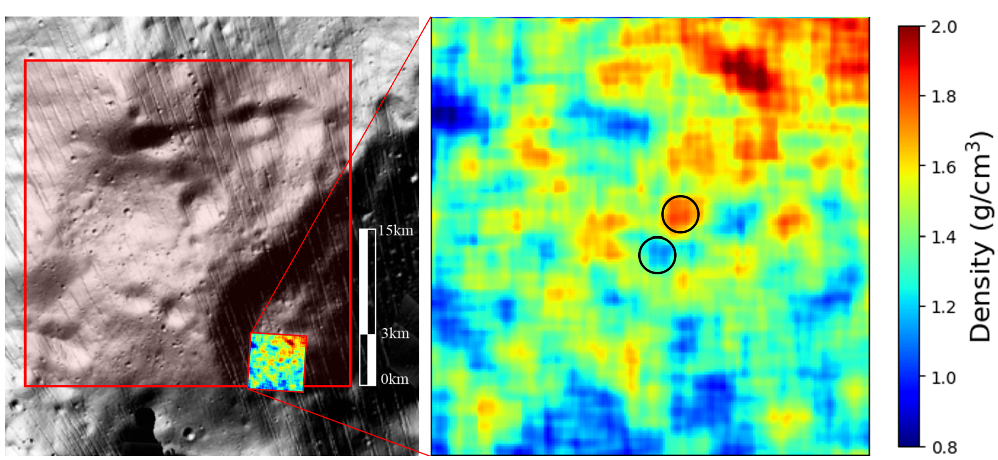

Fig. 7 Haworth Landing Site Bulk Density Estimation in Context (g/cm^3)

IV. Hazard Relative Navigation

A. State of the Art

While the use of global-positioning systems has dramatically simplified navigation on and near Earth, a similar capability is not yet available for missions to the Moon. Instead, terrain relative navigation (TRN) is a pivotal navigation technology that guides landers to their final destination in a precise and safe manner. Given the varied surfaces of planetary bodies, TRN allows landers to navigate the terrain and find their landing site by comparing real-time images of the surface to pre-existing maps. Notably, TRN was demonstrated successfully on the Mars 2020 spacecraft depositing the Perseverance rover onto the Martian surface. The recent IM-1 mission by Intuitive Machine's Nova-C lander also used the technology successfully to land on the moon within 1.5 km of the target location [23]. The general concept of terrain relative navigation has a high technological readiness level, but there are certain goals set by NASA for technological improvements of TRN technologies that have yet to be developed. The first is to design a TRN sensor that can map a planetary surface effectively in real-time during descent within dark, shadowed, or illuminated regions. Having technology that is independent of surface lighting will help modern landers land anywhere and at any time without constrictive lighting requirements. The second is to take advantage of modern technologies and sensor capabilities to facilitate technology transfer into NASA's instrumentation suite. The third is to solicit public-private partnerships and use commercial off-the-shelf (COTS) sub-systems to accelerate developmental timelines. These three goals for NASA's precision landing and hazard avoidance (PL&HA) technology gaps are all supported by HINDER radar instrumentation within Phase 1 (Hazard Relative Navigation) of the HINDER Concept of Operations [24].

B. Instrumentation System Design

A key aspect of the HINDER system is that it characterizes high-PSI susceptible sites as landing hazards, in the same way that large rocks, steep slopes, craters, and other surface objects that violate HLS-R-0071 requirements are considered landing hazards [21]. HINDER integrates an instrumentation system onto the HLS lander to identify high-PSI susceptible sites during descent and image the lunar surface to decrease landing risk and meet the three aforementioned PL&HA goals. The instrument is designed to not only meet the HINDER mission requirements, but also contribute to Artemis and HLS goals as well. Table 2 depicts additional requirements and objectives for the instrument to contribute to the greater goal of the Artemis missions.

Table 2 Instrumentation System Requirements [25]

Artemis Science Objectives	Human Landing System Goals		HINDER Goals	Science Objectives	Direct or Enabling	Scientific Measurement Requirements: Physical Parameters	Scientific Measurement Requirements: Observables	Mission Requirement
Investigation 1f-1: Determine the physical properties of regolith at diverse locations of expected human activity	6.2.2 Environmental Modeling	Monitoring of debris entrained by rocket plumes	Real Time High-PSI Susceptibility Hazard Detection	Measuring geotechnical characteristics of the landing zone	Direct	Dielectric Constant	Landing site susceptability to PSI	HINDER Phase 1-2
					Enabling	Bulk Particle Density		
	6.2.3 Understanding the human impact on the moon	Characterize resultant surface contamination from HLS landing plume	Post-Landing Validation		Direct	Dielectric Constant	Changes in surface characteristics during and post-plume impingement	HINDER Phase 3-4
					Enabling	Bulk Particle Density		

In selecting a remote sensing technology for measuring dielectric constant, various sensor types and operating modes were evaluated. Passive sensors, such as lidar and optical cameras, were compared to active sensors such as radar (Appendix 6). While passive sensors typically have lower weight and power consumption requirements, radar is selected for HINDER due to the proven ability to estimate the bulk density of lunar regolith through measurement of dielectric constant. Radar is also capable of operating with no performance loss in dark, shadowed, or illuminated regions on the surface. The ability to function independently of surface lighting allows for any-time landings, a necessary characteristic for when launch cadences are increased in the future. As mentioned in Section III.C, the Mini-RF radar is a TRL 9 instrument used aboard LRO and Chandrayaan-1 that is used for imaging the lunar surface and all Artemis candidate sites. While Mini-RF is a compact-polarimetric radar which transmits circularly polarized radar and receives a linearly polarized signal, HINDER is anticipated to use dual-polarized elements to achieve full-polarization and conserve mass and power compared to a compact-polarimetric radar. While this may require the use of a different model to estimate surface dielectric constant than is used for Mini-RF data, high accuracy models are also available for linearly polarized radar [12]. The calculations for key sizing values showcased in Table 3 are included in Appendix XI.B.

Table 3 High-Level Radar Parameters

Requirement	Value
Frequency	24 GHz
Wavelength	12.5 mm
Antenna Size	0.36x0.36 m
Estimated Total Mass	15-25 kg
Beamsteering	Electronic
Beam-Angle Range	0-30 degrees
Beam Width	3.1-3.5 degrees
Number of Elements	1024
Total Power	20 W
Antenna Efficiency	30%
Transmit Power	114.8 dBm
Pulse Width	10 ns

For HINDER's radar operating mode, a K-band phased array radar scatterometer is used to obtain high resolution (low beam width) point measurements of the surface. This frequency selection is driven by the mass availability of commercially-off-the-shelf (COTS) systems that can be applied for HINDER's purpose. Automotive radars are standardized to two frequency's: 24 GHz and 77 GHz. Because a current NASA science objective is to obtain regolith bulk density down to at least 20 cm, the choice of 24 GHz is made to meet that requirement [26].

The approach of using a phased array radar as a scatterometer has been extensively demonstrated and validated through commercial automotive systems. These system are designed to meet rigorous standards for reliability, precision, and durability. Even with existing high technical standards, continuous advancement within the automotive industry have increased radar resolution and signal processing capabilities. While HINDER requires more phased array elements and a higher transmitting power than that of commercial automotive systems, the design approach and sizing methods of these systems can be leveraged.

The digital beam forming of a phased array radar allows the beam to be steered and map the lunar surface without mechanical actuation and allows the radar to operate at lander angles up to 30° from to the site being targeted. This minimizes the integration requirements that the HINDER instrumentation places on the lander and does not require any changes to the lander guidance, navigation, and control (GN&C) system. If this field of view is insufficient based on the planned lander trajectory, the instrument can be mounted at an angle to the lander base to take advantage of the full 60° cone field of view.

C. Calibration (Phase 1)

The initiation of the instrumentation system occurs during descent, at approximately 1km altitude. At the same height, other PL&HA systems activate concurrently. Due to HINDER's antenna beam width, dielectric constant data resolution is only better than existent data below an altitude threshold of 490m, no matter the lander. This operational limit is not a constraint on the overall performance of the system because from initiation to an altitude of 490m, a calibration procedure is performed to confirm nominal operations of the system. By leveraging a process similar to TRN but with imaged dielectric constant data, HINDER can verify whether collected data matches expected returns based off of existing data. Any anomalous signals received shall trigger an object differentiation process which uses a suite of signal processing methods to filter out abnormal results. At the same time, imaging returns are saved locally and transmitted back to Earth once touchdown is complete for future analysis. This process is called hazard relative navigation (HRN) and is a critical redundancy feature to ensure that radar returns during the next phases will accurately guide the lander towards a safe site. Figure 8 depicts a high-level overview of the radar logic in Phase 1.

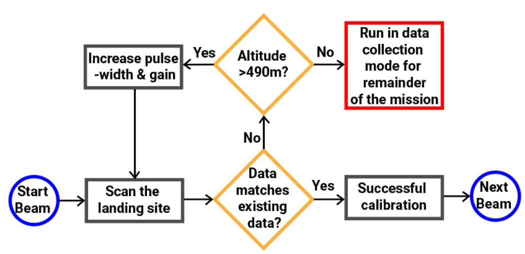

Fig. 8 HRN Logic Flowpath

V. Hazard Detection and Avoidance

A. State of the Art

Current hazard detection and avoidance (HDA) sensors and technologies in use on CLPS landers autonomously identify landing hazards and direct the lander to a safe location in real-time during final descent. Remote sensing instruments from orbiters have limited resolution, and autonomous landers require as much data as possible ensure a safe landing. Intuitive Machine's Nova-C landing during IM-1 in February of 2024 required a safe landing site no smaller than 10 meter by 10 meter, but existing data does not support resolution that high [23]. Multiple sensors such as optical cameras for crater recognition, lidar for surface slope detection, inertial measurement units (IMU) for positioning, and others contribute to the active detection of and navigation to a safe landing site. However, multiple technological gaps and areas for improvement exist within current HDA capabilities. Real-time mapping technologies for hazard detection and avoidance during lunar descent all the way until landing is a current developmental focus driven by NASA. Additional instrumentation to append to fused-sensor maps and advanced algorithms to aid in landing-site identification are both goals also recognized by the administration [24].

Sensor fusion is the process of merging data from different sensors to create a more accurate and comprehensive understanding of the environment. Data from diverse sensors such as optical cameras, lidar, radar, ultrasonic, inertial measurement units, and others is integrated together to create a comprehensive understanding of the terrain. To accomplish this, each sensor feeds data into a virtual processing unit (VPU), a computing platform within the command and data handling (CD&H) subsystem. The VPU then processes the data and forms hazard maps, which are cost maps that determine the danger of landing at a site within the range of the map. Figure 9 shows examples of hazard maps generated by a lidar-based system which captures elevation, slope, and roughness data of an equivalent area.

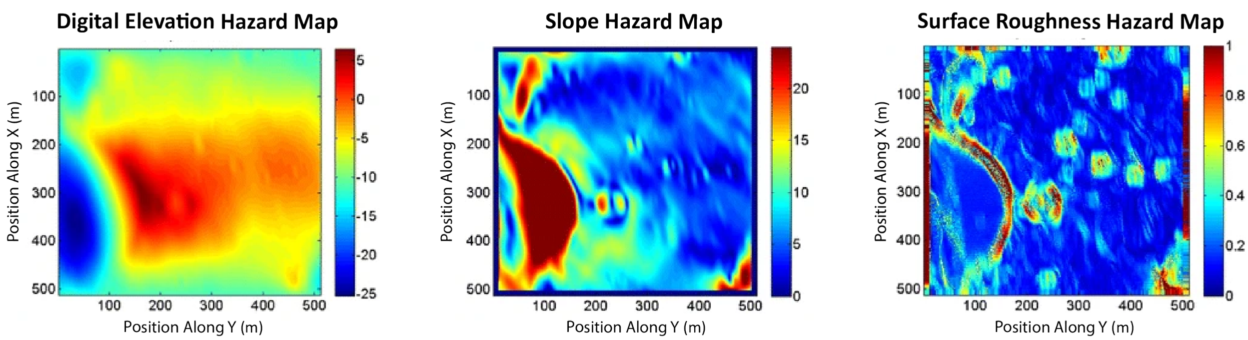

Fig. 9 Hazard Map Examples [27]

The VPU then integrates all hazard maps to form a singular fused hazard map, completing the sensor fusion process. Each graph has a different range of values due to the respective parameter it is depicting. Sensor fusion normalizes all of the different values to one singular scale. Figure 10 shows the output from the sensor fusion process with the three previously shown hazard maps as inputs.

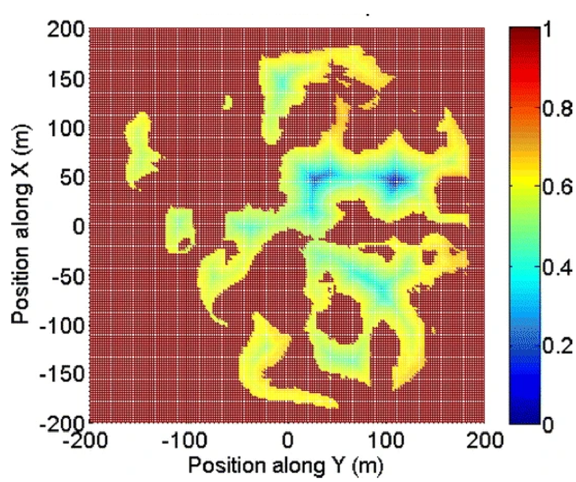

Fig. 10 Fused Hazard Map Example [27]

Because the final output is a cost map, the landing site with the least cost is the most desirable for landing. The areas masked with a red plaid pattern fall out of the preliminary requirements set for a safe landing and thus are not considered. The fused hazard map is constantly updated throughout flight, until a designated altitude threshold is met. The final coordinates are then sent to the central processing unit, or CPU, to be then processed using GN&C algorithms and converted into flight maneuvers.

B. Architecture and Operations

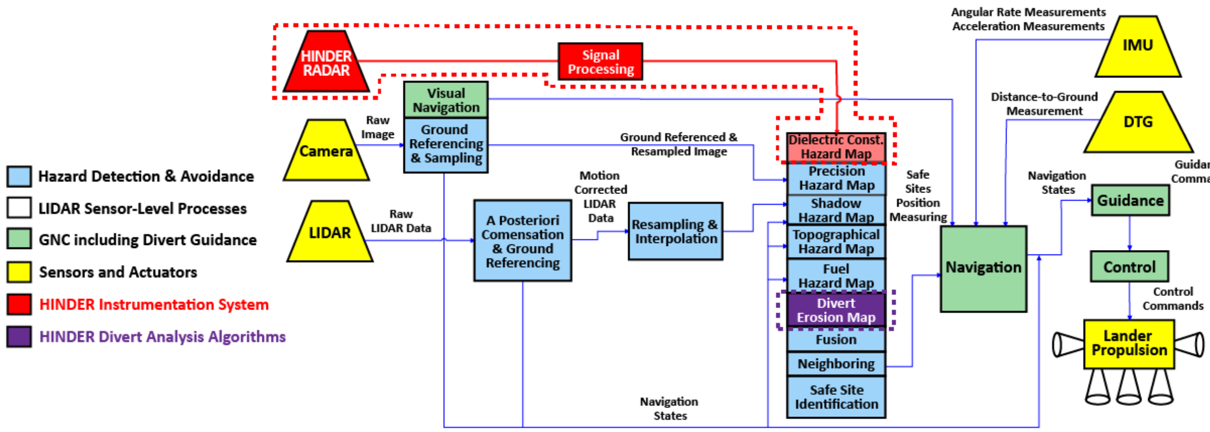

Fig. 11 HINDER HDA Architecture

HINDER integrates into HLS's existing Hazard Detection and Avoidance (HDA) architecture by providing additional hazard maps of bulk density and divert-induced erosion into the existing landing site selection process. The fused hazard maps generated by the lander's sensors and HINDER's instrument are used to calculate the safest landing point in the area, which is then fed into the guidance, navigation and control system, commanding the divert maneuver towards the chosen site. To do this, the existing navigation system generates a new trajectory which is delivered to the the guidance system, enabling existing flight control system to generate the necessary commands for the lander's control systems. This architecture ensures that HINDER can be added on to any existing GNC system using sensor fused HDA maps without significant modification. Figure 11 showcases how HINDER integrates into a typical HDA architecture with the additions to the hazard map and control block. Figure 12 expands on how HINDER integrates with navigation and guidance processes.

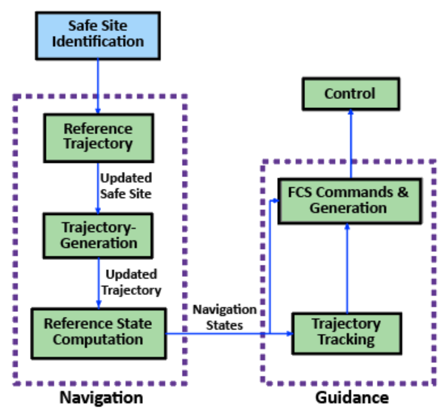

Fig. 12 GNC Integration

C. Active Hazard Avoidance (Phase 2)

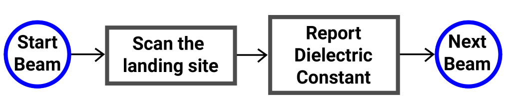

Fig. 13 HDA Logic Flowchart

Once the lander descends below the 490m threshold and the HRN process detects no data anomalies, Phase 2 begins. Here, resolution from the radar becomes higher than that of existing data and thus, higher-fidelity landing decisions can be made. As the lander approaches terminal descent, the bulk density hazard map shown in Figure 11 is constantly updated with newly processed radar data imported from the VPU. This real-time hazard detection process is crucial to make the most well-informed landing decision within the performance bounds of the radar system. Figure 13 depicts a high-level overview of the radar logic during the real-time hazard detection process. The bulk density maps alone, however, cannot be used to conduct diverts, as the act of diverting also impacts erosion and PSI. Hence, it is necessary to create an additional hazard map that accounts for the PSI cost of diverting to another location. While the bulk density hazard map is computed during flight, the divert hazard map can be created using simulations before flight as a function of altitude and accessed from memory. Like the bulk density hazard map, this divert hazard map is integrated into the existing set of HDA hazard maps to minimize the changes to the HLS guidance and control system while still positively impacting the trajectory to mitigate PSI effects.

D. Landing Divert Analysis

As a low-fidelity demonstration of this concept, a set of example divert hazard maps were created using Roberts' model. While this model is relatively simple, it is sufficient to demonstrate the concept. For a full implementation on HLS, more complex and accurate state of the art PSI models and simulations will be used. As preliminary validation for this approach, these simulation results were compared against experimental data from the PSI research laboratory at the University of Illinois. Setting the variables of the simulation used for the HINDER divert map demonstration to match the lab conditions, the simulations accurately replicated the experimental data within acceptable margins. The expanded results of this validation are available in Appendix XI.D, and the parameters of the analysis and the sub-scale experiment parameters are described in Appendix XI.C. In this context, the units h/D, x/D and z/D represent non-dimensional heights and distances where h, x, z and D refer to height, x-axis distance, z-axis distance and nozzle diameter, respectively.

As a proof-of-concept, all simulations assume the lander uses a single vertical nozzle and executes a slant divert at each point of the map. This type of trajectory, which is a popular basic maneuver from literature, offers a simplified model of divert maneuvers [28]. This maneuver allows the simulations to remain within the assumptions of Roberts' model. In this analysis, it serves as a baseline for understanding erosion mechanics in more complex divert trajectories. This analysis also uses two-dimensional models to identify bounds to the domain and a three-dimensional model for the full cost maps.

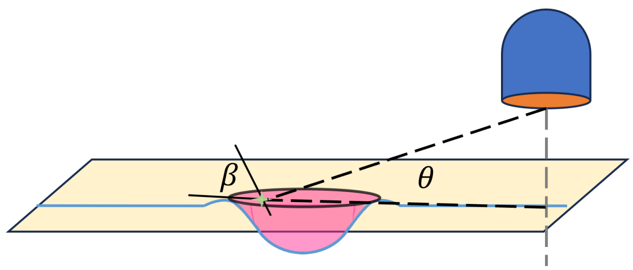

Fig. 14 Three dimensional Implementation of Roberts' model

While the two-dimensional Roberts' model simulation is based off code originally developed by the University of Illinois PSI lab, a divert implementation and a three-dimensional simulation were developed by the HINDER team [29]. Within Roberts' model, the erosion due to a nozzle at a given position is a function of β, the local slope angle, and θ, the azimuth angle. Converting this to three dimensions, the two-dimensional math of Roberts' model can be extended to three dimensions by treating each point on the surface as part of an independent two-dimensional model, as shown in Fig. 14. This was also used to simulate a moving thruster. The conditions are the same as shown in Appendix XI.C.

E. Landing Site Divert Bounds

For these simulations, Roberts' model was used to model crater erosion rate as a function of engine and trajectory parameters, including height above the surface, chamber pressure, nozzle radius, chamber temperature, and exit Mach number. Variables such as nozzle radius, chamber temperature, and exit Mach number are constant for each landing, whereas chamber pressure and height above the surface vary throughout the trajectory. Figure 15 showcases the relationship between erosion rate and height for the various maximum chamber pressures expected from past lunar landers [30]. The specific values for this analysis are included in Appendix XI.C, and all lengths are non-dimensionalized by division by the nozzle diameter, D. From initial analysis, it was identified that the erosion rate spikes in between an order of 10^0 and 10^1 h/D of altitude. Hence, the majority of the surface erosion is dictated by the activity below the $100h/D$ mark. As a result, any maneuvers and aborts above this altitude would not significantly impact PSI cratering. This finding is supported by simulation work done by the Marshall Space Flight Center in support of the Firefly Aerospace Blue Ghost Lander [7, 31].

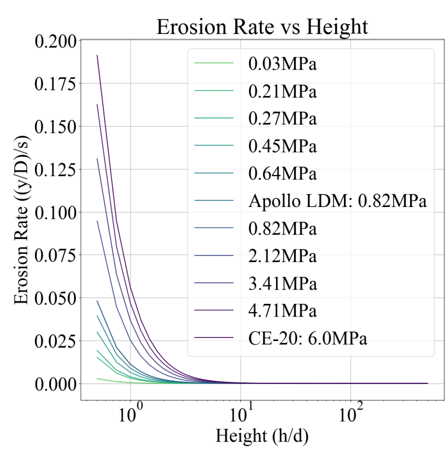

Fig. 15 Erosion rate vs height

These findings were then used to bound low-fidelity Roberts' model simulations of diverts for a divert impact hazard map concept demonstrate. The parameters for the divert are stated in Table 4. While the results of the divert hazard map demonstration are somewhat dependent on these values, the principle of the divert hazard map concept can be applied for any lander configuration with an HDA system.

Table 4 Divert Parameters

Parameter	Value
Initial Descent Height	$100\frac{h}{D}$
Divert Height	$[90, 50, 10]\frac{h}{D}$
Divert Distance in x and z axis	$[0, 10, 20, ..., 100]\frac{x/z}{D}$
Descent Velocity	$1(\frac{h}{D})/s$
Divert Velocity	$20(\frac{x}{D})/s$

F. Divert Hazard Map Concept Demonstration

As a concept demonstration of divert hazards maps for PSI impacts, a set of hazard maps was simulated for non-dimensionalized heights of 90, 50, and 10 h/D, which are shown in Fig 16. These maps represent the hazard map evolution over a lander's descent. Based on this simplified application of Roberts' model for a homogeneous surface, the simulation results imply that a divert at a high altitude (near $90h/D$) not only decreases the cost compared to that of a lower divert, but also may reduce volumetric erosion relative to a purely vertical descent. This is likely because under viscous erosion theory and Roberts' model, a flat surface erodes slower than a sloped surface. Additionally, increasing the altitude decreases erosion regardless due to the greater distance from the surface, providing the additional benefit of a high diversion. Therefore, conducting a high altitude diversion over flat ground results in lower overall erosion when compared to that of its lower altitude counterpart.

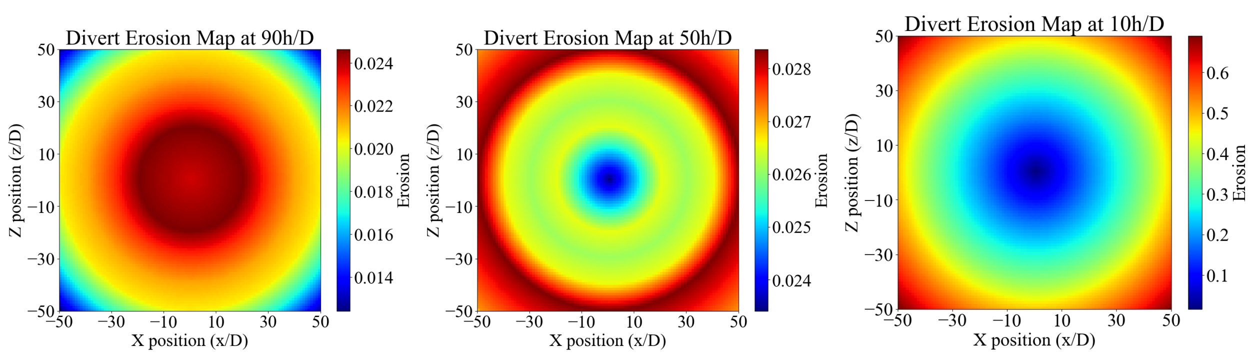

(a) 90h/D Altitude **(b) 50h/D Altitude** **(c) 10h/D Altitude**

Fig. 16 Divert Hazard Maps

At lower altitudes, a divert maneuver becomes more costly in terms of total volume eroded, which is expected due to higher erosion rates. The transition when diverts become less beneficial seems to occur between 90 and 50 h/D, however this threshold is a function of the specific lander, surface characteristics, and simulation model used. The pre-flight analysis for this hazard mapping does not take into account non-uniform surface topology or other uncertainties in the surface which will be encountered. Thus, this analysis can be further refined during flight using the data gathered about surface topology from HINDER and other HDA instruments. This includes, in the future, landing proximity to surface assets, which could be negatively weighted. Through further analysis, either during flight or with higher fidelity pre-flight simulations, the specific threshold within which diverts are beneficial to erosion can be determined. Through these initial findings, it can be seen that the divert-induced erosion map, within the HDA system, provide the guidance and navigation with the ability to effectively reduce PSI effects over the course of a landing.

VI. Surface Measurement and Ascent

Once a landing site is selected by the PL&HA system and terminal descent begins, the HINDER radar instrumentation can either be deactivated to prioritize power for other PSI instrumentation or it can continue operating in a data collection mode. If power is available, the instrument continuously records radar measurements of the selected landing site all the way through touchdown on the surface and shutdown of the landing engines. Through analysis of this data following the mission, it may be possible to gain new insights into how the plume impacts surface characteristics and dielectric properties throughout the landing process, including changes to the upper regolith density due to erosion. While this data may not be available to guide the final part of the descent due to plume and dust interference with the radar, the change in radar reflectivity of the landing site from initial measurements during hazard detection to measurements taken on the surface after landing could provide insights into the impacts of the landing on the local geology that are not obtainable by other instrumentation.

Similarly, while the proposed instrumentation system cannot be used for hazard detection or avoidance on ascent from the lunar surface at the end of the mission, it can be used to re-survey the landing zone and nearby areas to characterize the changes caused by landing and surface activity. These measurements could provide additional context to visible spectrum imagery of changes to the surface and long range measurements of the changes caused by ascent, though the extent to which radar measurements would detect surface changes as a result of PSI will require further analysis.

One of the biggest challenges surrounding current plume-surface-interaction research is the uncertainty within the existing soil model. By leveraging the instrument to find the bulk density of the landing zone before and after erosion begins, erosion rates and crater shapes can be correlated with the measured soil properties, and further PSI modeling efforts will have access to additional soil model information.

VII. Test Campaign

Due to the aggressive timeline and the relatively short foundational phase (Figure 3), HINDER requires a rigorous verification and validation process. Initial testing during the exploratory phase and early part of the foundational phase includes software-in-the-loop and hardware-in-the-loop verification tests. Given the importance of integration and test for PSI instruments such as Ejecta STORM, a significant emphasis is paced on this effort for HINDER in order to meet the target schedule.

The system needs to the be tested over a series of field tests using flight-like profiles that are expected during the descent phase. Additional testing to stress operational modes outside of the expected descent trajectories are also performed. In order to conduct these initial tests terrestrially, a variety of equipment is used to cover the large span of altitudes and velocities that the lander and system experience during descent. A high-performance jet can be used for high-altitude high-velocity testing to simulate Phases 1 & 2, whereas a helicopter can be used for low-altitude low-velocity testing to simulate Phases 3 & 4. Precedence in using such aircraft to simulate flight profiles terrestrially has been established by the Mars Terminal Descent Sensor (TDS) team. The TDS is a pulse-doppler landing radar that was used aboard the Mars Science Laboratory spacecraft to aid in determining when and where it was safe to lower the Curiosity rover to the ground. Jet Propulsion Laboratory (JPL) engineers involved with the TDS program integrated the instrument onto an F/A-18 aircraft and Eurocopter AS350 helicopter to test instrument performance by simulating expected flight profiles. With the TDS program showing promising test results and a rapid design/integration timeline, HINDER utilizes a similar terrestrial testing campaign [32]. By performing these tests early in the development process and often to iterate on the design, HINDER aims to reduce the risks in integrating the system and identify potential issues early in development. In addition to functional and performance testing on aircraft, HINDER instrumentation and software solutions are intended to begin preliminary integration with HLS as early as possible. This will allow the system to be designed with greater knowledge of the limitations of HLS, and will allow potential integration issues to be identified before they become critical.

For the underlying simulations and modeling supporting the creation of hazard maps, the models shall be validated as they are generated by the relevant investigators. For example, bulk density estimation hazard maps generated by the Mini-RF team using existing radar data are expected to be validated by the team processing the data and producing the resulting data product.

VIII. Cost Analysis

Using existing NASA costing tools, two cost estimates were generated for HINDER, providing a bounded range. The high end of the range was created using NASA's Instrument Cost Model (NICM). NICM is a JPL cost-modeling tool that uses mass and power-driven Cost-Estimating Relationships (CERs). The total cost projection using this method is $14.8 million, which is broken down into $9.9 million for the sensor itself and $4.9 million of programmatic costs, including integration and test. This estimate is expected to be the high end of the range, as the NICM CERs are based on heritage instrument development. Since HINDER is similar to traditional systems on Earth, it is expected to have lower development costs.

To take into account the similarity between the HINDER instrument and existing commercial systems such as automotive radar, a cost estimate was conducted by comparing to existing radar systems. A hardware cost of $\$500,000$ was assumed, and NASA CERs were used to estimate the programmatic and software costs. This method returned a forecasted cost of $1.36 million, forming the lower bound estimate. The final estimated cost for HINDER is between 1.36 and 12.78 million USD. This range also includes the cost of developing the bulk density and divert hazard maps, which are likely to be done by NASA or in close collaboration with NASA teams. Figure 17 summarizes the cost per year and breaks down each cost category: design and development, fabrication, integration and testing.

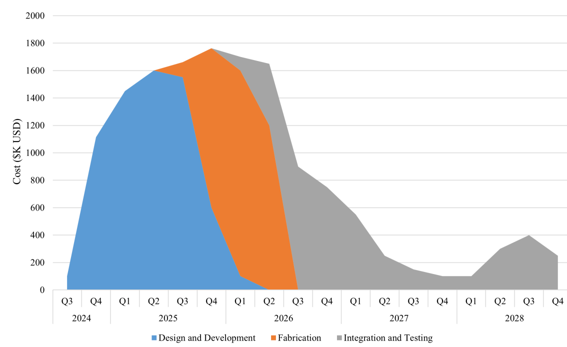

Fig. 17 Cost Breakdown

IX. Risk Analysis

HINDER minimizes risk through its flexibility in design and scope, as well as its realistic integration into existing HLS systems. Rather than requiring entirely new systems or procedures, HINDER leverages the work already being done for HLS through the hazard detection and avoidance system and builds on it in a way that can be easily disabled in the event of an anomaly. The greatest risk to HINDER is programmatic, with the redirection of funding to other HLS instruments. To mitigate this, HINDER can be slowly implemented over multiple phases over multiple missions, allowing the costs to be spread out while continually improving HLS safety to a significant extent with each step.

To reduce risks in the flight systems, pathfinders are developed to be used on terrestrial test beds to validate performance in flight like conditions. A precursor mission on Artemis III is also planned to verify the performance of the full-scale product. HINDER is also designed to be minimally invasive to the HLS's PL&HA system, adding only to its hazard maps that feed into respective GN&C systems.

Fig. 18 Pre-Mitigation (Left) and Post-Mitigation (Right) Risk Matrix

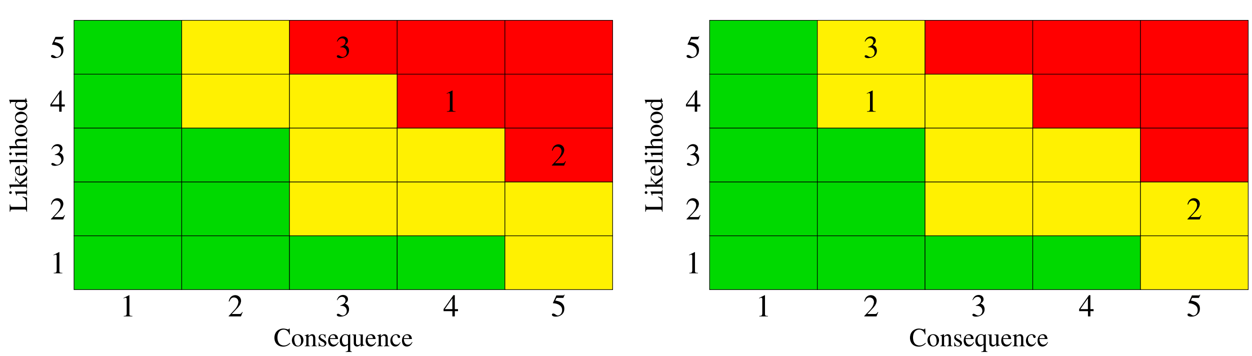

Table 5 Risk and Mitigation Table

ID	Risk	Mitigation
1	Given the limitations on funding for PSI instrumentation, there is a risk that funding is redirected to other instruments adversely impacting the resources available to implement the design and leading to the instrument not being available for a mission.	HINDER uses a flexible scope and timeline to implement PSI erosion reduction in multiple steps, allowing for a gradual buildup of capability if required.
2	Given that S-band radio is used for communications between Artemis assets, there is a risk that the frequencies used expand beyond the current guidelines, resulting in the potential for interference from the radar and requiring the radar to be redesigned to accommodate a different frequency.	Preliminary design is agnostic of exact frequency used, with final frequency selection being made after communications frequencies are disclosed. The narrow beam width of the radar also significantly reduces the side-lobe interference to the communications system.
3	Given that HINDER must integrate with HLS hazard detection system, there is a risk of software testing failure, adversely impacting mission readiness and leading to cost and schedule increases.	The HINDER elements of the hazard detection system can be easily disabled, allowing the mission to proceed with the HINDER systems in a data recording mode in the event of integration delays.

X. Conclusion

After more than half a century, humanity will once again set foot on the Moon with Artemis III. HINDER will play a crucial role in ensuring astronauts' safe return by mitigating the threats originating from ejecta and cratering. To supplement current hazard relative navigation and avoidance systems for HLS, HINDER uniquely proposes two phases of radar-based surface characterization and landing site selection. This selection starts with mission planning based on existing lunar data sets and further refines this selection in flight with an active phased-array radar system that measures dielectric constant in real-time to avoid hazardous landing sites with high PSI-susceptibility. HINDER also proposes trajectory deviations that are processed and initialized during the hazard detection and avoidance phase for diverts away from hazardous sites. These diverts to locations with higher bulk density further minimizes ejecta, safeguarding critical instrumentation and the lander.

Taking full advantage of all flight systems included in the HINDER design, the proposed solution supports long term PSI research by measuring and informing a better understanding of soil bulk density and its correlation to erosion, enabling an increase in fidelity for PSI and surface modeling lunar soil models. Better soil models lead to more confidence in technologies developed on Earth for the moon.

HINDER is not only within compliance of the 2024 Human Lander Challenge requirements, but also contributes to the closure of technological gaps within NASA's PL&HA instrument suite. With HINDER's innovative approach, the Artemis missions are poised to overcome lunar surface challenges and ensure the safety and success of humanity's return to the Moon.

Acknowledgements

The team would like to acknowledge our advisor Dr. Laura Villafañe Roca for her advice and support. We would also like to acknowledge Nicolas Rasmont for participating as a reviewer in the design reviews as well providing technical assistance in understanding Roberts' model and sensor design. A large gesture of appreciation goes to Dr. Robert Maddock of NASA's Langley Research Center for his tremendous insight into the SCALPSS program which influenced a significant amount of HINDER's operations and logistics. The team would also like to thank the Illinois Space Society's technical director, Galen Sieck and former RASC-AL project manager Alec Auster for their review and feedback on the design. The team is also thankful to Robert Barthell for helping us design the visuals and video for HINDER. Finally we would like to thank Rick Eason from the Laboratory for Advanced Space Systems at Illinois (LASSI) for his input on the adaptability of commercial radar systems to cislunar applications.

XI. Appendices

A. Roberts' Model Expansion

Roberts' model is stated by Hutton [3]:

$$\frac{\partial y}{\partial t} = \frac{2(\tau - \tau^*)}{au \cdot \sigma c \cdot \cos(\beta)} \tag{1}$$

However to conduct the Monte Carlo and trajectory analysis, the individual components need to be expanded to calculate the erosion rate using soil and engine parameters. The shear stress (τ) is expanded as:

$$\tau = C_f q \tag{4a}$$

Here, q is the dynamic pressure, which can be calculated using the following formula:

$$q = \frac{\gamma}{\gamma - 1}\left[1 - \left(\frac{p}{p_s}\right)^{\frac{\gamma-1}{\gamma}}\right]\left(\frac{p}{p_s}\right)^{\frac{1}{\gamma}} p_s \tag{4b}$$

p is the ground pressure, which is calculated as:

$$p = p_s \cos(\theta)^{k+4} \cos(\beta)^2 \left(1 - \tan(\theta)\tan(\beta)\right)^2 \tag{4c}$$

Here p_s is the stagnation pressure, which is calculated using the following formula:

$$p_s = \frac{k+2}{2}\left(\frac{r_e}{h}\right)^2 p_r \tag{4d}$$

Here p_r is the post-shock recovery pressure, which is calculated using the following formula:

$$p_r = \frac{\left(1 + \gamma M_e^2\right) p_c}{\left(1 + \frac{\gamma-1}{2} M_e^2\right)^{\frac{\gamma}{\gamma-1}}} \tag{4e}$$

The shear restraining stress (τ^*) is expanded as:

$$\tau^* = \sigma c D g \cos\beta \tan\alpha - \sigma c D g \sin\beta + \frac{A_{coh}}{D^3} + \tau_{coh} \tag{5}$$

The momentum factor (a) is expanded as:

$$a = \frac{1}{0.5 + \sqrt{0.25 + \left(\frac{1}{18}\frac{\mu_c h}{\sigma D^2 \sqrt{RT_c}\,(k+4)}\left(1 + \frac{(k+2) D C_d p_r}{72\sqrt{2}\mu_c\sqrt{RT_c}}\left(\frac{r_e}{h}\right)^2\right)\right)}} \tag{6a}$$

k is the hypersonic simularity parameter, which is calculated as:

$$k = \gamma(\gamma - 1) M_e^2 \tag{6b}$$

C_d is the friction coefficient of particles, which is estimated to be:

$$C_d = \frac{24}{Re_D} \tag{6c}$$

Re_D is the particle's Reynolds number, which is calculated as:

$$Re_D = \frac{\rho u D}{\mu} \tag{6d}$$

μ is the gas viscosity. which is calculated as

$$\mu = \mu_c \left(\frac{p}{p_s}\right)^{\frac{\gamma-1}{2\gamma}} \tag{6e}$$

u is the velocity parallel to surface, which is calculated as:

$$u = \sqrt{2\gamma \left(\frac{RT_c}{\gamma - 1}\right) \left(1 - \left(\frac{p}{p_s}\right)^{\frac{\gamma-1}{\gamma}}\right)} \tag{6f}$$

ρ is the gas density, which is calculated as:

$$\rho = \frac{2q}{u^2} \tag{6g}$$

B. Instrument Trade Studies & Requirements

Sensor Type	Accuracy	Penetration Depth	Resolution	Weight & Power Requirements	Data Processing Complexity	Integration Capability with Trajectory Profile
Radar	High	Moderate	High	Moderate	Moderate	Medium
Lidar	Low	Low	High	Low	Low	High
Optical Cameras	Low/None	None	High	Low	Low	High

Table 6 HINDER Instrumentation Technology Selection

	Low Frequency Radar	High Frequency Radar	Optical/Infrared Laser
Frequency	2 – 30 GHz	30 – 300 GHz	0.4 – 400 THz
Wavelength scale	cm	mm	µm
Resolution	Low	Medium	High
Ground/dust penetration	High	Low / None	None
Transmitter size	High	Medium	Low

	Phased Array (PA) Synthetic Aperture	Phased Array (PA) Real Aperture	Single Synthetic Aperture	Single Real Aperture
[Example]	PA-SAR	PA-Scatterometer	GPR	Scatterometer
Resolution	1°<BW<4°	0.5°<BW<1.5°	15°<BW<17.5°	0.5°<BW<1.5°
Beam Steering	Digital	Digital	Mechanical	Mechanical
Power Consumption	High	Medium	Low	Low
TRL	8	8	6-9	7

	Phased Array Synthetic Aperture	Phased Array Real Aperture	Single Synthetic Aperture	Single Real Aperture
Beam Steering	Digital	Digital	Mechanical	Mechanical
Beamwidth	TBD	0.5° - 1.5°	TBD	0.5° - 5°
Power Consumption	High	Medium	Low	Low
TRL	8	8	6-8	7

Table 7 HINDER Radar Trade Studies

To size the radar antenna, it is assumed that all elements are square and have a spacing of $\lambda/2$. Based off analogous 24GHz radar systems, HINDER's elements are 5mm x 5mm. With a wavelength of 12.5mm, the following equations show how antenna sizing was achieved:

The element width E_w is defined as:

$$E_w = \frac{5}{1000}\ \mathrm{m} \tag{7}$$

To get 1024 total elements, the number of elements on each side of the antenna, n, is given as:

$$n = 32 \tag{8}$$

The length of one side of the antenna given in meters is calculated by:

$$L_m = n \cdot E_w + n \cdot \frac{\lambda}{2} \tag{9}$$

Given one side, the total area can then be calculated by:

$$A = L_m^2 \tag{10}$$

To make sure the radar has enough penetration depth this equation is used:

$$d = \frac{\sqrt{\varepsilon_{\text{real}}}}{2 \cdot \pi \cdot \varepsilon_{\text{imaginary}}} \cdot \lambda \tag{11}$$

The relationship between $\varepsilon_{\text{real}}$ & $\varepsilon_{\text{imaginary}}$ is given by:

$$\tan(\delta) = \frac{\varepsilon_{\text{imaginary}}}{\varepsilon_{\text{real}}} \quad \text{(degrees)} \tag{12}$$

Instrument mass was found by comparing two current systems. One of the systems, ROLSES, is a low-wavelength radar with a small antenna. It is assumed that HINDER, since it requires a larger antenna, has a larger mass than ROLSES. The mass of ROLSES's entire system is 14.8kg [33]. The larger system is the Mars Terminal Descent Sensor (TDS). The TDS uses 6 fixed antennas compared to the 1 phased array antenna used for the HINDER radar instrument.

C. Parameters for Trajectory and Divert Analysis

The parameters inputted into the Roberts' model for the trajectory and divert analysis are shown in the following tables. These numbers are based on the sub-scale laboratory conditions described by Rasmont et al. [29]. These laboratory numbers were used to provide verification for simulation results. These numbers were preferred over other lander numbers due to Roberts' model's scaling nature and the accuracy of the sub-scale descriptions. We prioritized accurate sub-scale parameters over inaccurate scale parameters.

Table 8 Exhaust Gas Parameters

Variable	Value	Meaning
R	$\frac{8.314}{0.028}$	$[\frac{J}{mol \cdot K}]$ universal gas constant, normalized by mass
γ	1.4	heat capacity ratio
μ_c	$17.49 \cdot 10^{-6}$	$[Pa \cdot s]$ viscosity in the rocket chamber

Table 9 Surface Geology Parameters

Variable	Value	Meaning
g	1.62	$[\frac{m}{s^2}]$ lunar gravitational constant
D	$109 \cdot 10^{-6}$	$[m]$ diameter of dust particles
c	0.6	packing concentration in dust layer
σ	2500	$[\frac{kg}{m^3}]$ density of dust particle
α	20	[deg] static angle of repose of cohensionless particles
$\alpha_{collapse}$	25	[deg] angle of repose at which avalanche start
K	1	shear stress augmentation factor

Table 10 Rocket Engine Parameters

Variable	Value	Meaning
r_e	0.005	[m] nozzle radius exit
M_e	5	nozzle exit mach number
p_c	$1.25 \cdot 10^6$	[Pa] max rocket chamber pressure
T_c	300	[K] temperature in rocket chamber

Table 11 serves as an overview of the crucial parameters influencing the descent and divert dynamics in the series of simulations done in divert analysis. The provided values contribute to a better understanding of the conditions and variables involved in the simulation. In the context of this discussion, the units h/D and x/D represent non-dimensional heights and distances where h, x and D refer to height, distance, and nozzle diameter respectively. Using the same framework, the descent and divert velocities are represented in non-dimensional units.

Table 11 Divert Parameters

Parameter	Value
Descent Height	$100\frac{h}{D}$
Divert Height	$[90, 80, 70, ..., 10]\frac{h}{D}$
Divert Distance	$[0, 50, 100, ..., 1000]\frac{x}{D}$
Descent Velocity	$10\frac{h}{D}/s$
Divert Velocity	$20\frac{x}{D}/s$

D. Validation of Roberts' Model

The team collaborated with the PSI group at the University of Illinois to validate Roberts' model with experimental data. The PSI group has a sub-scale experimental facility, shown in Fig. 19a, which consists of a vacuum chamber and cold gas thruster as described by Rasmont et al. [29]. They provided the HINDER team with experimental data of the craters that result from their lunar test regime. The HINDER team validated our implementation of Roberts' model by comparing it to the available lab data shown in Fig.19b. Using the exact lab conditions, we replicated the final crater for their implementation of Roberts' model and our implementation of lateral translation and compared them to the lab data. Through this, we determined that our simulations accurately replicate experimental data to an acceptable extent. The crater slope and dimensions (height and diameter) are seen within acceptable range. Additionally, Fig. 19b demonstrates that our implementation replicates the standard model in the static nozzle case. The implementation of lateral translation involved removing the expectation of an axisymmetric crater from the standard model. We remove this expectation by assuming that the surface pressure distribution remains as described by Roberts because $y << h$, i.e. the crater depth is much less that nozzle height above the surface. Hence, our implementation of lateral translation does not violate the base case which builds confidence in its use.

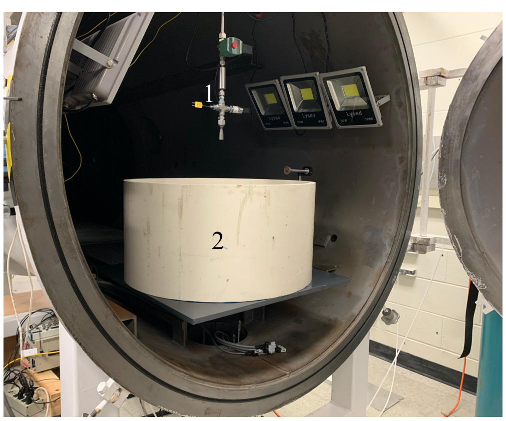

(a) UIUC PSI Experimental Facility (Courtesy of Dr. Roca)

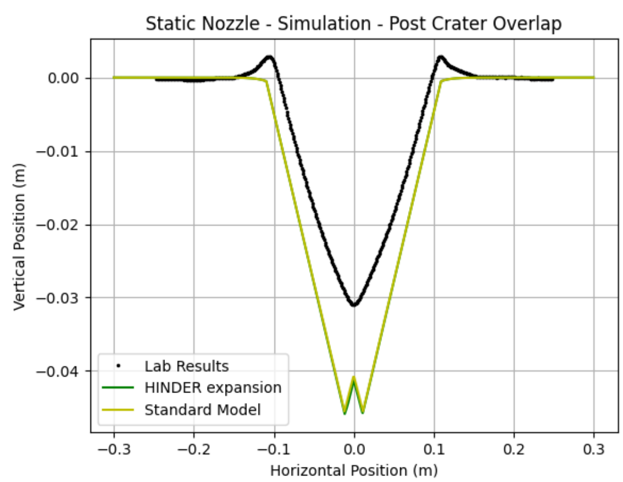

(b) Simulation vs Lab Results

Fig. 19 Validation of Roberts' Model

E. Code

All the simulation programs as well as the code used to generate the figures shown in this paper can be found at `https://github.com/ISSUIUC/HuLC_2024_UIUC`

References

[1] Maddock, R., "FY23 GCD CLPS PSI Mini-Suite Annual Review Presentation," , 2023. URL `https://ntrs.nasa.gov/citations/20230013095`.

[2] Roberts, L., "The action of a hypersonic jet on a dust layer," Tech. rep., NASA, 1963.

[3] Hutton, R. E., "Comparison of soil erosion theory with scaled LM jet erosion tests," Tech. rep., NASA, 1968.

[4] Metzger, P. T., Lane, E., J., and Immer, C. D., "Modification Of Roberts' Theory For Rocket Exhaust Plumes Eroding Lunar Soil," *Earth and Space*, 2008.

[5] Metzger, P., "Erosion rate of lunar soil under a landing rocket, part 1: identifying the ratelimiting physics," *Icarus*, 2024.

[6] Metzger, P., "Erosion rate of lunar soil under a landing rocket, part 2: benchmarking and predictions," *Icarus*, 2024.

[7] West, J., Liever, P., Weaver, A., Shurtz, T. P., Gale, M., Krolick, W. C., and Griffin, L. W., "Overview of the Predictive Simulation Capability Element of the Plume Surface Interaction Project," *AIAA SCITECH 2022 Forum*, 2022. URL `https://arc.aiaa.org/doi/abs/10.2514/6.2022-2319`.

[8] Korzun, A. M., and Chambers, W., "Development Efforts and Status of Plume-Surface Interaction Capabilities for Propulsive Landing Systems," , 2024.

[9] Heiken, G., Vaniman, D., and French, B., *Lunar Sourcebook: A User's Guide to the Moon*, LPI contribution, Cambridge University Press, 1991. URL `https://books.google.com/books?id=7Q49AAAAIAAJ`.

[10] Metzger, P., Smith, J., and Lane, J. E., "Phenomenology of soil erosion due to rocket exhaust on the Moon and the Mauna Kea lunar test site," *JOURNAL OF GEOPHYSICAL RESEARCH, VOL. 116*, 2010.

[11] Feng, J., Siegler, M., and White, M., "Dielectric properties and stratigraphy of regolith in the lunar South Pole-Aitken basin: Observations from the Lunar Penetrating Radar," *Astronomy and Astrophysics*, 2022.

[12] Campbell, B., *Radar Remote Sensing of Planetary Surfaces*, Cambridge University Press, 2002.

[13] D. W. Strangway, G. R. O., G. W. Pearce, "Magnetic and Dielectric Properties of Lunar Samples," Tech. rep., Departments of Geology and Physics University of Toronto, 1977.

[14] Kumar, A., Kochar, I. M., Pandey, D. K., Das, A., Putrevu, D., Kumar, R., and Panigrahi, R. K., "Dielectric Constant Estimation of Lunar Surface Using Mini-RF and Chandrayaan-2 SAR Data," *IEEE TRANSACTIONS ON GEOSCIENCE AND REMOTE SENSING*, 2022.

[15] Calla, O., Mathur, S., and Jangid, M., "Comparision of Dielectric Constant of Apollo 17 Samples With Mini-RF & Tals," *Large Meteorite Impacts and Planetary Evolution V*, 2013.

[16] Singh, A., Sharma, A., Kumar, S., Chang, L., Vashishtha, A., Raj, R., Agrawal, S., and Chauhan, P., "Dielectric characterization and polarimetric analysis of lunar north polar crater Hermite-A using Chandrayaan-1 Mini-SAR, Lunar Reconnaissance Orbiter (LRO) Mini-RF, and Chandrayaan-2 DFSAR data," *Advances in Space Research*, 2022.

[17] Gao, Y., Dang, Y., Lu, P., and Hou, W., "Investigating the dielectric properties of lunar surface regolith fines using Mini-RF SAR data," Tech. rep., National Key Laboratory of Microwave Imaging Technology, 2022. URL `https://www.sciencedirect.com/science/article/pii/S092427162300014X`.

[18] Bhattacharya, A., Porwal, A., Dhingra, S., De, S., and Venkataraman, G., "Remote estimation of dielectric permittivity of lunar surface regolith using compact polarimetric synthetic aperture radar data," *Advances in Space Research*, 2015.

[19] Rivera-Valentín, E. G., Fassett, C., Denevi, B., Meyer, H., Neish, C., Morgan, G., Cahill, J., Stickle, A., and Patterson, G. W., "Mini-RF S-band Radar Characterization of a Lunar South Pole–crossing Tycho Ray: Implications for Sampling Strategies," *The Planetary Science Journal*, 2024.

[20] Patterson, G. W., Stickle, A. M., Morgan, G. A., Fassett, C. I., and Thomson, B. J., "Availability of LRO Mini-RF Data for Artemis Landing Zone Characterization," *Lunar Surface Science Workshop*, 2023. URL `https://www.hou.usra.edu/meetings/lunarsurface20/pdf/5015.pdf`.

[21] NASA, "Human Landing System (HLS) Requirements Document," *George C. Marshall Space Flight Center*, 2019.

[22] Fa, W., Wieczorek, M., and Heggy, E., "Modeling polarimetric radar scattering from the lunar surface: Study on the effect of physical properties of the regolith layer," *Journal of Geophysica Research*, 2010.

[23] Lederer, S., "Intuitive Machines 1 (Odysseus)," , 2024. URL https://nssdc.gsfc.nasa.gov/nmc/spacecraft/display.action?id=IM-1-NOVA.

[24] "LAND: Precision Landing and Hazard Avoidance," , 04 2024. URL https://www.spacetechpriorities.org/wp-content/uploads/2024/04/LAND-Precision_Landing_and_Hazard_Avoidance_50m-2023-08-17.pdf.

[25] "Artemis 3 Science Definition Team Report," , 2015. URL https://www.nasa.gov/wp-content/uploads/2015/01/artemis-iii-science-definition-report-12042020c.pdf.

[26] Mitchelle Munk, C. N., Robert Maddock, "SCALPSS Project Overview," , 2020.

[27] Neveu, D., Mercier, G., Hamel, J.-F., Simard Bilodeau, V., Woicke, S., Alger, M., and Beaudette, D., "Passive versus active hazard detection and avoidance systems," , 2015. URL https://link.springer.com/article/10.1007/s12567-015-0074-4.

[28] May, Z. D., "Trajectory Shaping of Lunar Descent Approach Phase for Human Landing Systems," , 08 2020. URL https://ntrs.nasa.gov/citations/20205001834.

[29] Rasmont, N., Bansal, I., Al-Rashdan, H., Elliott, G., Rovey, J. L., and Roca, L. V., "Millimeter-Wave Tomographic Interferometry of Ejecta Concentrations in Plume-Surface Interactions," *AIAA SCITECH 2024 Forum*, 2024. URL https://arc.aiaa.org/doi/abs/10.2514/6.2024-1979.

[30] Polifka, R., "NASA PROGRAM APOLLO WORKING PAPER NO 1195," Tech. rep., NASA, 1966.

[31] Tyrrell, O. K., Thompson, R. J., Danehy, P. M., Dupuis, C. J., Munk, M. M., Nguyen, C. P., Maddock, R. W., Fahringer, T. W., Krolick, W. C., Weaver, A., West, J., Manginelli, M. S., and Witherow, W. K., "Design of a lunar plume-surface interaction measurement system," *AIAA SCITECH 2022 Forum*, 2021. https://doi.org/10.2514/6.2022-1693, URL https://arc.aiaa.org/doi/abs/10.2514/6.2022-1693.

[32] James F Montgomery, e. a., James Bodie, "Implementing the Mars Science Laboratory Terminal Descent Sensor Field Test Campaign," , 03 2014. URL https://ntrs.nasa.gov/citations/20140001971.

[33] Burns, D. D., "CLPS and Payloads Update," , 2020. URL https://smd-cms.nasa.gov/wp-content/uploads/2023/04/Burns_APAC_CLPSAPPayloadUpdate_Oct2020_TAGGED.pdf.